JOURNAL OF SPACECRAFT AND ROCKETS
Vol. 29, No. 6, November–December 1992

Computational Flow Predictions for Hypersonic Drag Devices

Susan Tokarcik* and Ethiraj Venkatapathy*
Eloret Institute, Palo Alto, California 94303

The hypersonic flows around two types of drag devices are analyzed using computational fluid dynamics. The mechanically deployed flares and inflatable ballutes are used to increase the drag of solid rocket motors, thereby assuring atmospheric capture during entry. To avoid the expense associated with thermochemical nonequilibrium solvers, computations were performed with an ideal-gas solver using an effective specific heat ratio to simulate real-gas effects. The ideal-gas solver is shown to predict drag comparable to that of the nonequilibrium solver when the effective specific heat ratio is chosen properly. A number of ideal-gas computations were performed to determine the sizes of the flare and ballute needed to achieve the required drag for atmospheric capture of the solid rocket motor. Qualitative comparisons of estimated heat transfer rates are made, and the best candidate designs based on total drag and estimated heat transfer rates are suggested.

Nomenclature

A_{ref} = reference area, πR_{case}^2, m^2
C_D = drag coefficient, $D/(q_\infty A_{ref})$
C_H = heat transfer coefficient, $\dot{q}_w/(0.5\rho_\infty U_\infty^3)$
C_P = pressure coefficient, $(p - p_\infty)/q_\infty$
D = drag, N
M = total mass, kg
L = length of flat plate portion of two-dimensional compression corner model, m
p = static pressure, N/m^2
p_∞ = freestream pressure, N/m^2
q_∞ = dynamic pressure, $0.5\rho_\infty U_\infty^2$, N/m^2
$\dot{q}_w$ = wall heat transfer rate, $-\kappa\Delta T/\Delta\eta$, W/cm^2
R_{case} = radius of solid rocket motor casing, m
Re = Reynolds number
T_∞ = freestream temperature, K
U_∞ = freestream velocity, m/s
X = distance, m
β = ballistic coefficient, $M/(C_D A)$, kg/m^2
γ_{eff} = effective specific heat ratio
ΔT = change in temperature
$\Delta\eta$ = change in normal distance from a wall
δ = flare angle or initial angle of ballute
γ = specific heat ratio, c_p/c_v
κ = thermal conductivity, cal/s-m-K
ρ_∞ = freestream density, kg/m^3

Introduction

THE use of supersonic and hypersonic drag devices, which are also referred to as decelerators, has been investigated for many years with applications ranging from high-performance re-entry vehicle recovery to booster-payload collision avoidance. The drag devices investigated in the present study are used to ensure that a solid rocket motor (SRM) casing jettisoned at the outer limits of the Earth's atmosphere does not skip along the upper atmosphere before beginning its final descent. This skip-out behavior makes the prediction of the Earth-impact point extremely difficult and is therefore undesirable.

The example SRM casing used in this study was designed for use with the aeroassist flight experiment vehicle (AFE) which was to execute a hypersonic aerobrake maneuver through the Earth's upper atmosphere. The AFE was to be deployed from the Space Shuttle in low-Earth orbit and to use the SRM to accelerate it to the necessary speed for the test. This scenario is shown in Fig. 1.

The jettisoned SRM casing is large and would not burn up entirely before reaching the Earth's surface. It is therefore necessary to accurately predict the Earth-impact point; thus skip-out must be avoided. The likelihood of skip-out can be determined by examining the ballistic coefficient, $\beta = M/(C_D A_{ref})$ (Fig. 2).[1] The ballistic coefficient of the SRM casing is approximately 137 kg/m^2. A ballistic coefficient of 49 kg/m^2 would ensure that skip-out does not occur[2] and also that the SRM casing would land in the water at least 300 miles from any large land mass. Since the mass M is fixed by the mission requirements and A_{ref} is assumed to be constant, the ballistic coefficient can only be lowered by increasing drag. This is accomplished by attaching a drag device to the SRM casing. To achieve the desired ballistic coefficient, the total C_D (C_D of the SRM casing plus C_D of the drag device) must be approximately 137/49 (= 2.8) times the C_D of the SRM casing without a drag device (C_D = 1.56). This corresponds to a C_D of approximately 4.5.

Supersonic and hypersonic drag device configurations that have been examined in the past include attached and tethered ballutes,[3–7] which are a combination balloon and parachute, and rigid flares,[8–12] among others. For this study, the attached ballute and the flare were chosen for the following reasons: 1) ease of decelerator deployment; 2) stability of the combined SRM casing and decelerator (SRM/decelerator) configuration; and 3) decelerator deployment during tumbling. Although both the ballute and the flare have been studied in the

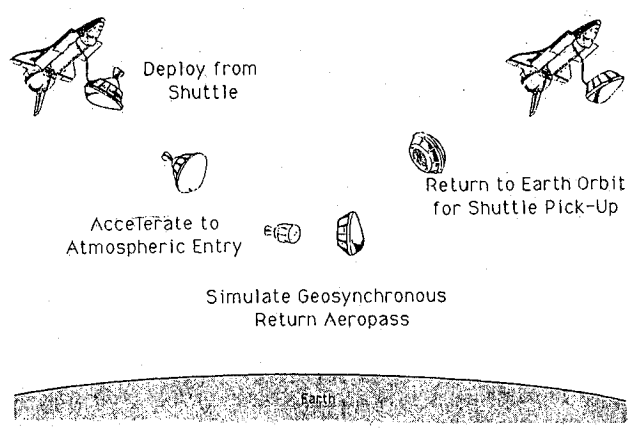

Fig. 1 AFE mission (NASA L-87-9597).

Received Dec. 31, 1991; revision received May 15, 1992; accepted for publication May 19, 1992. This paper is declared a work of the U.S. Government and is not subject to copyright protection in the United States.

*Research Scientist; mailing address, NASA Ames Research Center, MS 230-2, Moffett Field, CA 94035. Member AIAA.

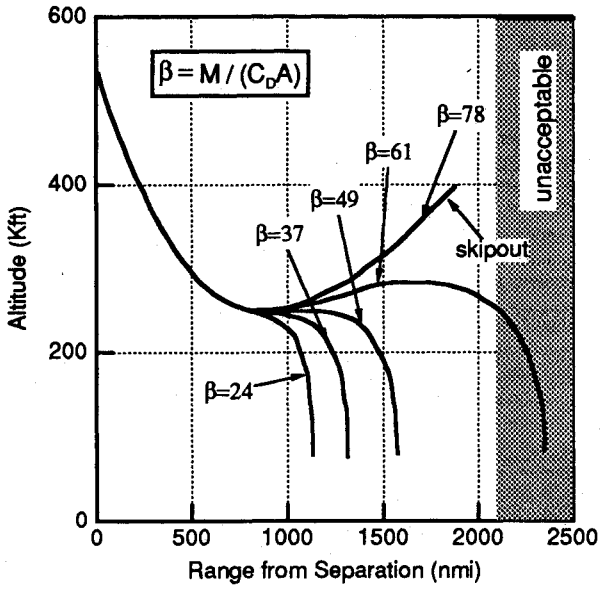

Fig. 2 Ballistic entry trajectories (Ref. 2).

past, these studies did not investigate the thermochemical nonequilibrium environment encountered along the SRM casing entry trajectory. It is very difficult, as well as expensive, to reproduce thermochemical nonequilibrium flowfields using ground-based experimental facilities. Therefore, computational fluid dynamics (CFD) was used to study the drag device flows.

Numerical Methods

The SRM/flare and SRM/ballute configurations used for the calculations are shown in Figs. 3a and 3b, respectively. A typical computational grid, 141 × 71 in size, is shown in Fig. 3c with every other point removed for clarity. Solution-adapted[13] grids were used to better refine important flow features. All calculations assumed axisymmetric flow, and the trajectory point chosen for the calculations corresponds to the peak heating trajectory point.[2] The freestream conditions are 1) altitude = 76,250 km, 2) $U_\infty = 9126$ m/s, 3) $\rho_\infty = 3.6087 \times 10^{-5}$ kg/m^3, 4) $p_\infty = 2.0674$ N/m^2, and 5) $T_\infty = 199.6$ K. The Reynolds number based on freestream conditions is 22,370/m, and the flow is assumed to be laminar. The baseflow region is not computed since the pressure in that region is very low and will not affect the total drag calculation.

A schematic of the major flow features is shown in Fig. 4. These features include the strong outer blunt-body shock produced by the nose of the SRM casing, a strong expansion region around the shoulder of the SRM casing, and the corner region formed by the juncture of the SRM casing with the drag device. The flow cannot negotiate the corner without separation and a recirculating region develops. The size of the separated region is important because a large separated region causes the drag device to be less efficient since the pressure within a separated region remains essentially constant and is lower than the inviscid limit. Also shown in Fig. 4 is a compression corner shock which is a weak shock caused by the initial flow separation. This shock interacts with the blunt-body shock and forms an oblique shock. The peak pressure and heat transfer rates for the drag devices occur in the vicinity of this shock-shock interaction region.

Thermochemical Nonequilibrium Solver

Because of the high altitude and high speeds of its trajectory, the flow around the SRM/decelerator may be in thermochemical nonequilibrium. Therefore, the flowfield is initially solved using a thermochemical nonequilibrium code developed by Palmer.[14] This code utilizes an explicit, finite difference, shock-capturing algorithm that employs flux-vector splitting to solve the thin-layer Navier-Stokes equations. The algorithm incorporates a finite-rate chemistry model consisting of ten species and a fully coupled two-temperature model.[15] The solutions predicted by this code have been successfully compared against ballistic range, shock tunnel, and flight data as well as solutions obtained with other nonequilibrium codes.[14] However, thermochemical nonequilibrium solutions are generally very costly, and Palmer's code required 3–4 h of CPU time on a Cray-2 for one SRM/decelerator calculation. It was therefore concluded that this type of solver was unsuitable for the current study which requires a large number of solutions.

Effective-γ Ideal-Gas Solver

To calculate solutions in a timely manner, an ideal-gas solver with an effective specific heat ratio, γ_{eff}, was used. By

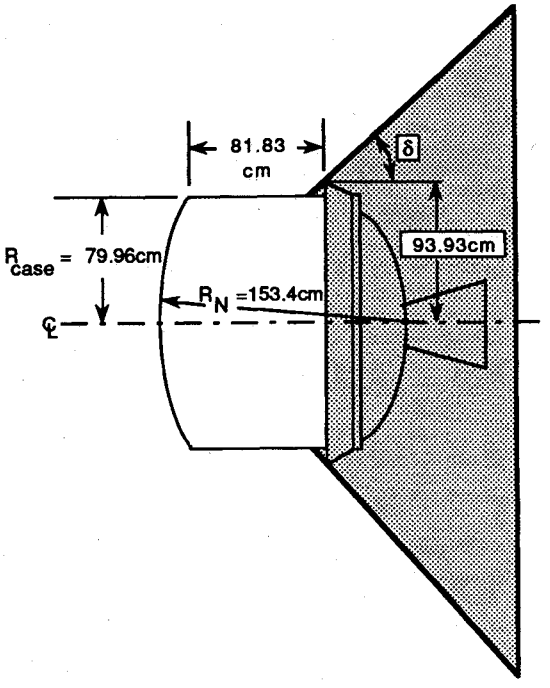

Fig. 3a SRM with flare drag device.

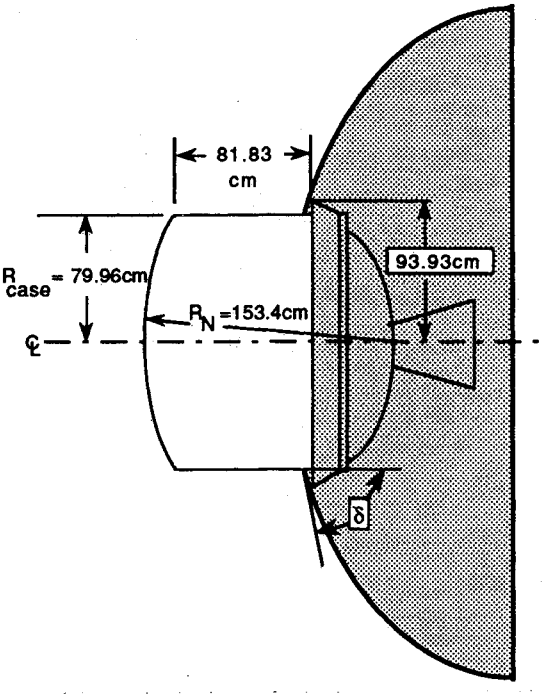

Fig. 3b SRM with ballute drag device.

using an effective value of γ, the pressure field of a real-gas flowfield can be simulated. This technique has been used successfully to predict drag and moment coefficients produced by blunt bodies in real-gas flows.[16] The ideal-gas code was developed by Candler[17] and has been modified by the authors to perform effective-γ calculations. The code uses an implicit, finite volume algorithm that utilizes a Gauss-Seidel line relaxation method to solve the thin-layer Navier-Stokes equations. Computed solutions have been compared against experimental data for spheres, blunt cones, and sharp-nosed cones at a variety of hypersonic speeds.[17] The ideal-gas solver is very robust and requires only 10–15 min of CPU time on a Cray-2 for an SRM/decelerator calculation.

The value of γ_{eff} used in the ideal-gas solver can be chosen by matching the calculated shock shape and standoff distance to those found by other methods (experiment or CFD) that incorporate thermochemical nonequilibrium effects at similar freestream conditions. Shock shape and standoff distance largely determine the pressure field of a flow and have therefore been chosen as the criteria for selecting the value of γ_{eff}. Since no experimental data exist for the SRM/decelerator flowfield, the results from Palmer's nonequilibrium code were used as the basis for the matching procedure.

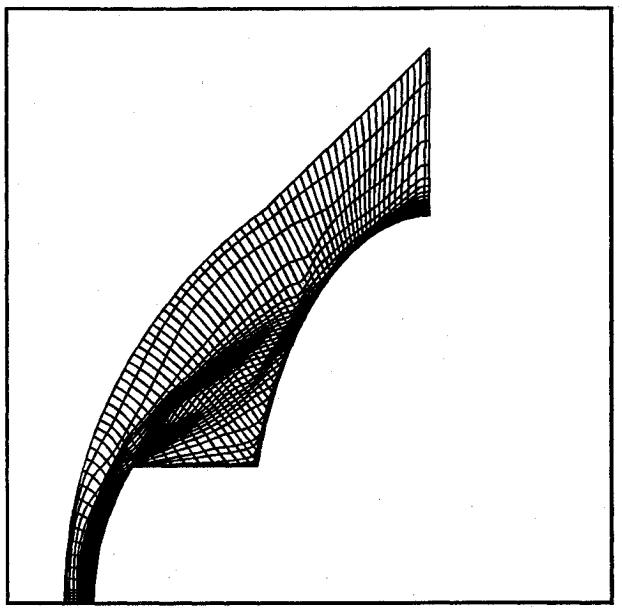

Fig. 3c Solution-adapted computational grid for ballute calculations.

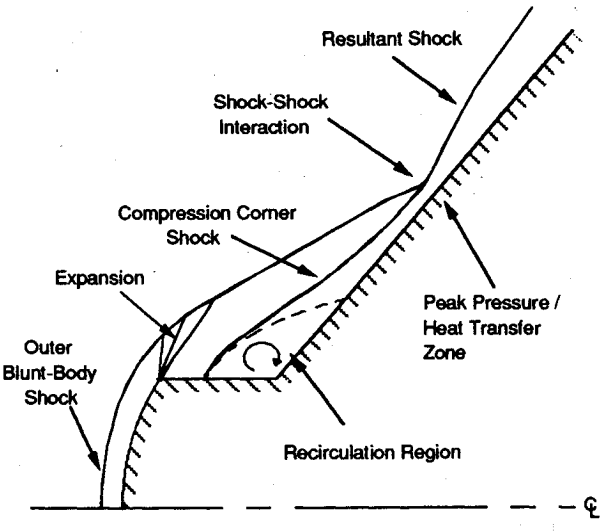

Fig. 4 Flowfield schematic for SRM and flare drag device.

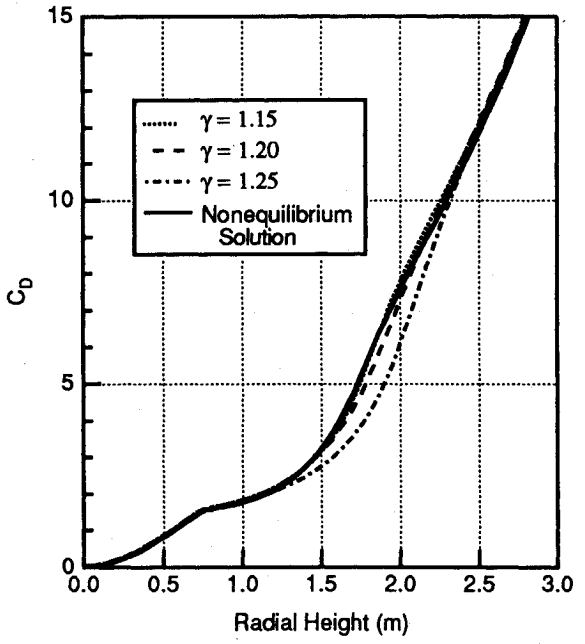

Fig. 5 Drag coefficient for variable γ and real-gas solution.

Ideal-gas solutions with a series of effective-γ were computed, and the resulting C_D curves are shown in Fig. 5 along with the nonequilibrium result. Since the calculation of drag is very important for this study, matching the nonequilibrium C_D curve was chosen as an additional criterion for selecting γ_{eff}. A γ_{eff} of 1.15 came closest to matching both the shock-shape and the shock-standoff criteria as well as the C_D criterion. The resulting pressure contours for the nonequilibrium calculation and the effective-γ calculation are shown in Figs. 6a and 6b, respectively.

Two-Dimensional Compression Corner Simulation

Palmer's nonequilibrium solver and Candler's ideal-gas solver have been used extensively for hypersonic blunt-body flows. However, neither had been used to study hypersonic flows with large separated regions. The size of the separated region can significantly affect the amount of drag produced by the decelerator and therefore must be predicted accurately.

Results from the ideal-gas solver are compared with experimental results for a two-dimensional, hypersonic compression corner flow.[18] In this experiment, the compression ramp was at an angle of 15 deg to the Mach 10 inflow, and the surface temperature of the model was maintained at 100 K. The test gas was air ($\gamma = 1.4$), and the freestream conditions were: $T_\infty = 50$ K, $p_\infty = 294.5$ N/m^2, and $Re_L = 2.3\text{x}10^6$, where L ($= 0.25$ m) is the length of the flat-plate portion of the model. The experiment was conducted at a relatively low Reynolds number in order to maintain laminar flow across the model; however, it appeared that turbulent transition may have taken place in the reattachment region. Since the values of surface pressure are of great importance to this study, calculated C_P from the ideal-gas solver are compared to experimental data in Fig. 7. The ideal-gas solver is able to predict the initial separation point, indicated by the pressure rise at $X/L = 0.82$, and the pressure plateau which is typical of a laminar separated region.[18] In the reattachment region the pressure overshoot, created by the interference between the separation and reattachment shocks,[18] is somewhat underpredicted by the ideal-gas solver. Since turbulent transition was reported to have taken place in this region, the underprediction seen in the computational results is expected.

The experiment also provided data for heat transfer rates, and the comparisons with computational values are presented in Fig. 8. The sequence of events for the heat transfer rates are as follows: 1) a slow decrease in the upstream part of the flat

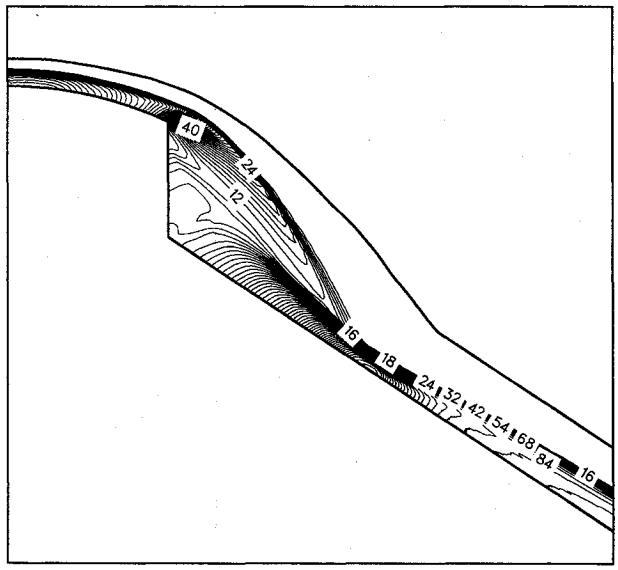

Fig. 6a Pressure contours ($= 0.1 \times p/p_\infty$): real-gas solution.

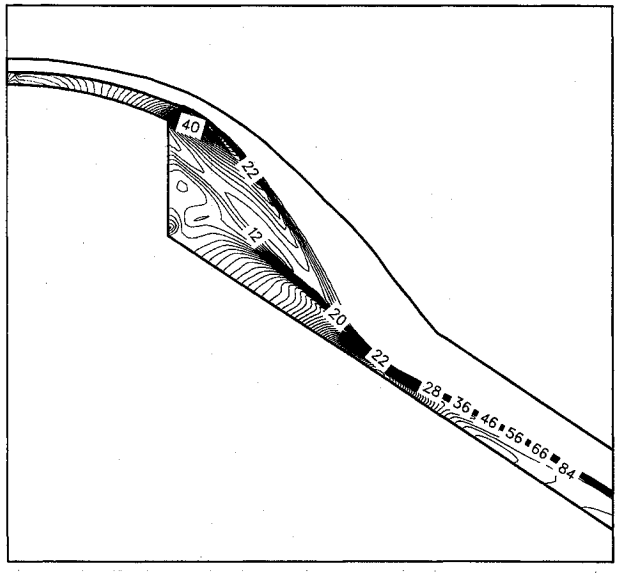

Fig. 6b Pressure contours ($= 0.1 \times p/p_\infty$): $\gamma_{eff} = 1.15$ solution.

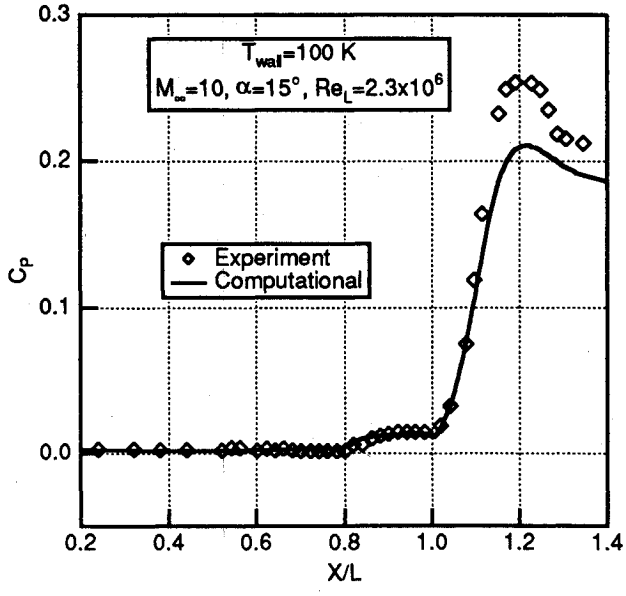

Fig. 7 Pressure coefficient for two-dimensional compression corner.

plate in accordance with the strong and weak interaction theory; 2) a more rapid decrease which is indicative of shock-induced laminar separation; 3) a minimum in the separated region; and 4) a peak value slightly downstream of the reattachment point. The calculated solution captures the first three events well, however the peak in the reattachment region is underpredicted. Again, the discrepancy is most likely caused by the lack of turbulence modeling in the ideal-gas solver.

In this report, the calculated heat transfer rates for the drag devices are presented only for qualitative comparisons between different drag device configurations. Quantitative comparisons are not appropriate for two reasons. The first has been discussed previously, i.e., the present analysis does not account for the effects of turbulence. The second reason is concerned with the ideal-gas assumption. In the actual nonequilibrium flow, the temperature profile is affected by chemical recombination in the vicinity of the cold wall. Since only one value of γ_{eff} is used for the entire flowfield, the variable real-gas effects near the wall are not well represented.

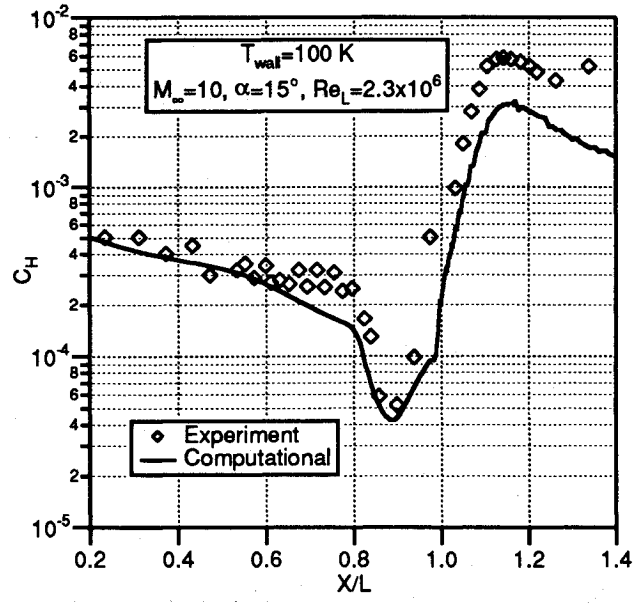

Fig. 8 Heat transfer rates for two-dimensional compression corner.

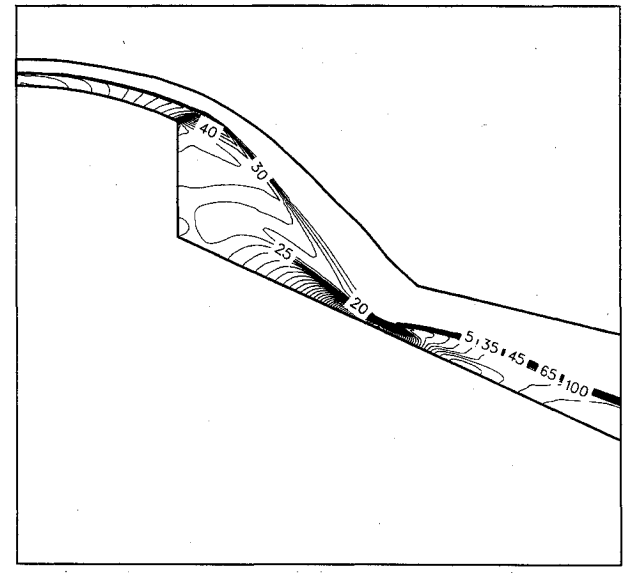

Fig. 9 Pressure contours ($= 0.1 \times p/p_\infty$)—60-deg flare with γ_{eff} = 1.15.

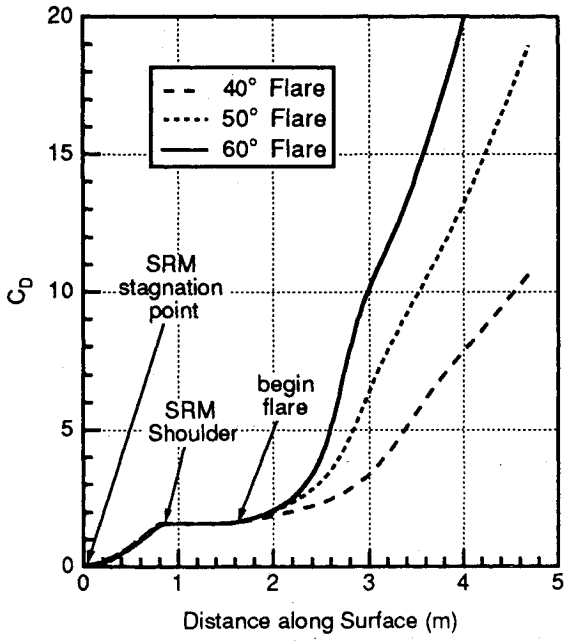

Fig. 10 Drag coefficient comparison for flares.

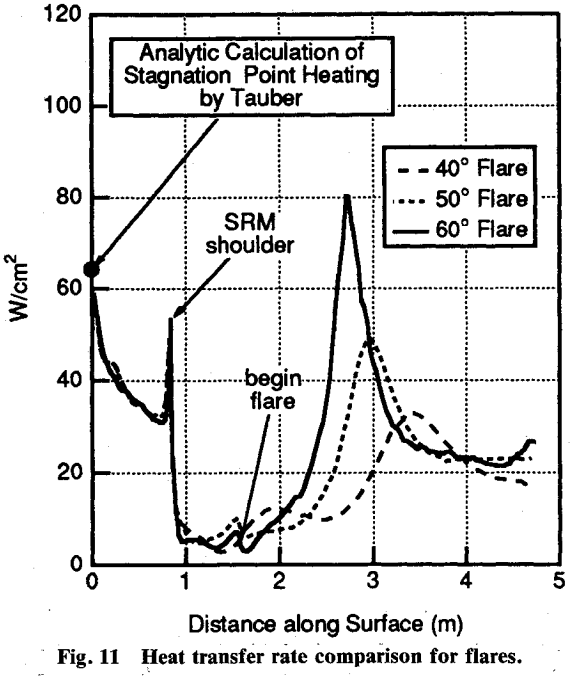

Fig. 11 Heat transfer rate comparison for flares.

Computational Results and Analysis

SRM/Flare Simulations

The first decelerator concept that is examined is the conical flare. A schematic of the flowfield produced by this type of configuration was shown earlier in Fig. 4 for a flare angle of 50 deg. The flare angle influences the size of the separated region and also the shape and strength of the shock downstream of the compression corner. Along with the size of the separated region, the strength of the shock produced by the compression corner of the flare also affects the efficiency of the decelerator. A strong shock produces a greater pressure rise than a weaker shock and therefore a greater increase in drag. Also, for larger flare angles, a greater portion of the pressure force vector acting on the body is directed in the axial, or drag, direction. This produces more drag for the same distribution of surface pressure.

Pressure fields for flare angles of 50 and 60 deg are shown in Fig. 6b and Fig. 9, respectively. The 50-deg flare produces a relatively large separated region. The initial separation is indicated by the clustering of pressure contours approximately one-third of the distance from the shoulder of the SRM casing to the compression corner, and the separation extends over approximately two-thirds of the SRM casing. Downstream of the shock-shock interaction region a resultant, oblique shock is formed. The peak pressure produced by this flare is of the order of that produced in the SRM nose stagnation region. When the flare angle is increased to 60 deg, a very large separated region is produced encompassing almost the entire SRM casing downstream of the expansion shoulder. But more importantly, the shock just downstream of the shock interaction region has changed from a weaker, oblique shock to a stronger, blunt shock before it finally becomes oblique. The effect of the strong shock is to produce a peak pressure on the flare that is much higher than the SRM nose stagnation-point pressure. The C_D calculated for 40-, 50-, and 60-deg flares are shown in Fig. 10. This comparison shows that the desired C_D of 4.5 can be achieved by any of these flares with the proper choice of flare length.

The computed heat transfer rates for the flare decelerators are shown in Fig. 11. The rise in heat transfer rate seen at 0.9 m along the surface is due to the thinning of the boundary layer as the flow expands around the shoulder of the SRM casing. The peak in the heat transfer rate in the flare region is due to the interaction of the bow shock and the shock produced by the decelerator. The maximum heat transfer rate to the flare is important since, for a ballistic coefficient of 49 kg/m^2, the decelerator must survive for approximately 120 s (Ref. 2) to ensure a successful mission.

As shown in Fig. 11, a 40-deg flare has a low heat transfer rate; however, it requires a greater length than the 50- or 60-deg flares to achieve the desired C_D. Therefore, an addi-

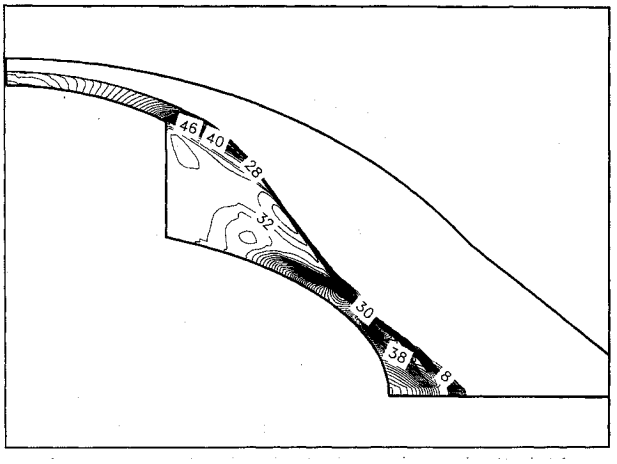

Fig. 12a Pressure contours ($= 0.1 \times p/p_\infty$)—75-deg ballute with $\gamma_{eff} = 1.15$.

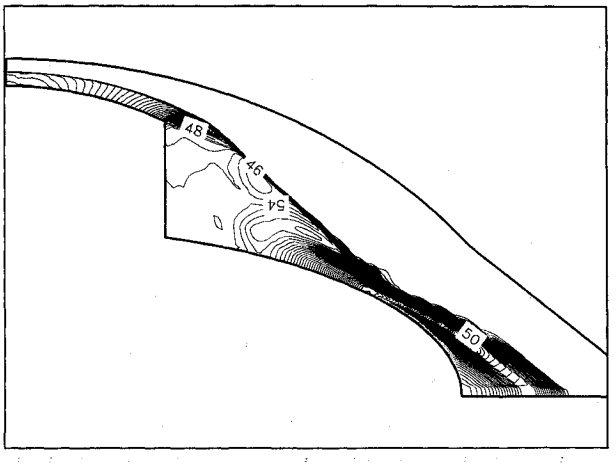

Fig. 12b Pressure contours ($= 0.1 \times p/p_\infty$)—80-deg ballute with $\gamma_{eff} = 1.15$.

tional mass penalty must be accepted. The 60-deg flare can achieve the desired drag with a shorter length, but it must also endure significantly higher heating rates compared to the smaller flare angles. This brings the survivability of the 60-deg flare into question. The 50-deg flare can achieve a C_D of 4.5 with a length only 20% larger than the 60-deg case. Furthermore, the 50-deg flare has a computed peak heat transfer rate which is considerably lower than for the 60-deg flare. Although the decelerator heat transfer rates are presented for qualitative comparisons, an analytical check of the SRM stagnation point heating rate was performed by Tauber using Ref. 19. This point is shown in Fig. 11 and is only 8% higher than that calculated by the ideal-gas solver.

SRM/Ballute Simulations

The ballutes studied here are ellipsoidal in shape and attach to the SRM casing with initial angles that vary between $\delta = 40$ deg and $\delta = 80$ deg. The ballutes produce strong, blunt shocks that interact with the bow shock off the nose of the SRM casing. This is in contrast to the flare drag devices which generally produce weaker oblique shocks. The interaction of the SRM bow shock and the ballute shock creates a high pressure region on the surface of the ballute. Downstream of this region the pressure drops off as the flow expands around the aft portion of the drag device. The flow in the region where the ballute attaches to the SRM casing is similar to the flare corner region.

Pressure contours for the 75- and 80-deg ballutes are shown in Fig. 12. The results for a 70-deg ballute, which produces a relatively small drag increase, are shown in Ref. 20. The pressure contours for the 75-deg ballute (Fig. 12a) show a larger separated region compared to the 50-deg flare case. The 75-deg ballute forms a strong blunt shock that interacts with the bow shock off the nose and produces a relatively small region of high pressure on the ballute surface. The pressure contours for the 80-deg ballute (Fig. 12b) also show a very large separated region, but a stronger shock is produced by this ballute. The interaction of the bow shock and the ballute shock produces a peak pressure that is considerably higher than for the 75-deg ballute. Also the area of the high pressure region on the surface of the 80-deg ballute is almost twice that for the 75-deg ballute.

The C_D computed for three ballute shapes are shown in Fig. 13. This comparison shows that although a 75-deg ballute can produce the desired drag increase ($C_D = 4.5$), the 80-deg ballute produces a C_D as high as 10 with only a modest increase

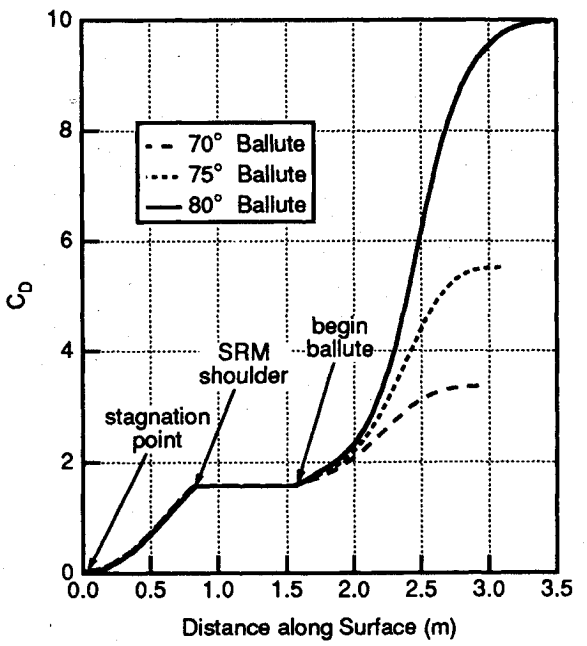

Fig. 13 Drag coefficient comparison for ballutes.

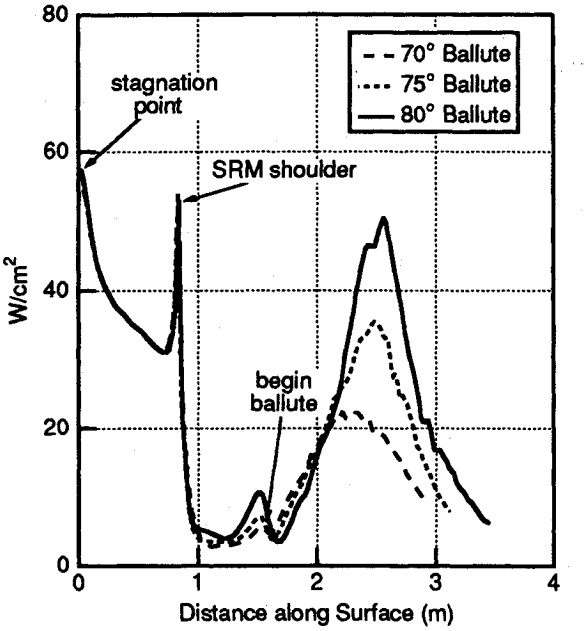

Fig. 14 Heat transfer rate comparison for ballutes.

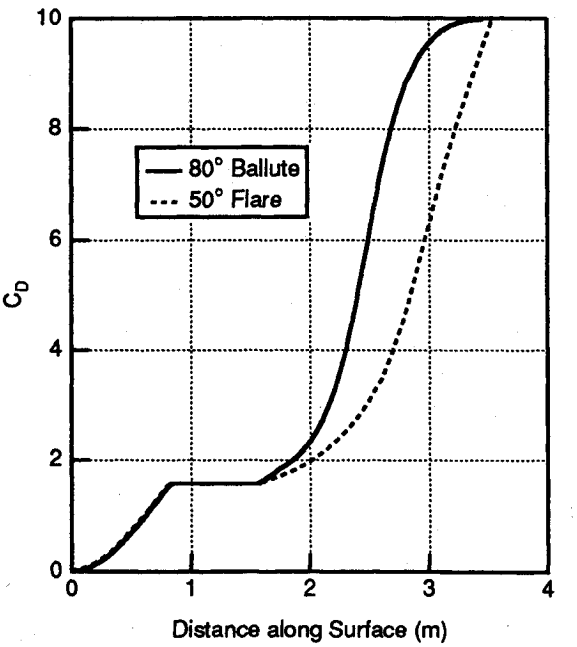

Fig. 15 Drag coefficient comparison for flare and ballute.

in size. In Fig. 14, it is shown that all of the ballutes have relatively low peak heat transfer rates. Wang and Shih[1] examined possible thermal protection materials for a ballute of similar design, and it is assumed that these materials also could be used for these designs.

Discussion

Comparisons of the C_D and heat transfer rates for the 50-deg flare and the 80-deg ballute are shown in Figs. 15 and 16, respectively. Overall efficiency is based on the surface length needed to achieve the desired drag increase, and the 80-deg ballute requires 2.41 m to achieve a C_D of 4.5 compared to 2.88 m for the flare. The ballute is more efficient than the flare despite having a larger separated region and an expansion surface at the aft end which produces little drag. The larger separated region is not a great disadvantage because the pressure within the separation is almost twice as high as the pressure within the flare's separation.

Other considerations may also be important when choosing a drag device design. For instance, because the ballute is

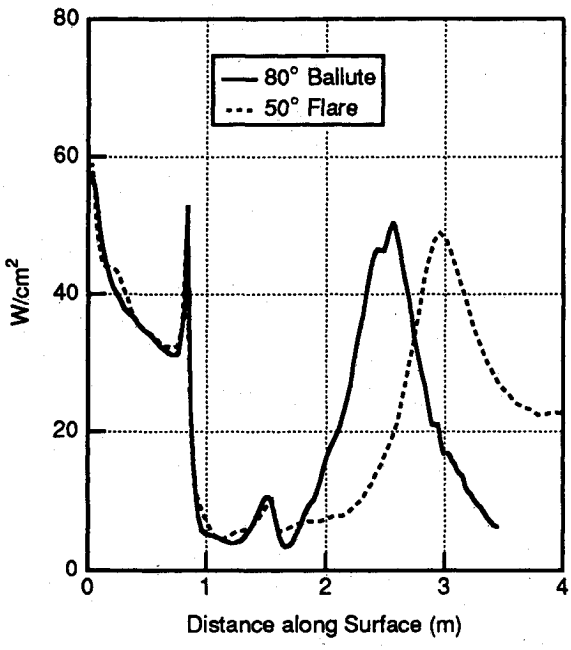

Fig. 16 Heat transfer rate comparison for flare and ballute.

inflated, it is possible for it to deform in regions of high pressure such as that produced by the shock-shock interaction discussed earlier. The flare consists of rigid members and would not be subject to such deformations. However, the maximum external pressure on the surface of the 80-deg ballute was computed to be only 0.04 atm. Because the external pressure is low, the ballute could be inflated to an internal pressure that is substantially higher in order to preserve its shape. Another problem that should be considered is the three dimensionality of the flow if the SRM/decelerator were to trim at some nonzero angle of attack. Although a solution to this type of problem requires a full three-dimensional calculation, some inferences can be made about the centerline pressure and heating by examining axisymmetric solutions with larger and smaller flare or ballute angles. For instance, the 40- and 60-deg flare solutions can be used to study the flowfield of a 50-deg flare at a 10-deg angle of attack.

It seems likely that a combination of the flare and ballute geometries could be constructed to take advantage of the desirable characteristics of the separate geometries. An optimization procedure could be performed to produce a geometry that minimizes the separation region, maximizes the total drag increase, and minimizes the heat transfer rates to the decelerator. An experimental optimization study would be expensive and time consuming as would a computational study utilizing a full thermochemical nonequilibrium solver. However, the effective-γ ideal-gas computational method used here is very well suited for such a design study. The computational procedure requires approximately 10 CPU min for each new design, and this time could be reduced with a judicious choice of initial conditions.

Conclusions

It has been shown that either a flare or a ballute can be used to produce an SRM/decelerator configuration with a total C_D large enough to prevent skip-out during descent. The 80-deg ballute is able to produce the required drag using 20% less surface length than the 50-deg flare for similar peak heat transfer rates.

Employing an effective-γ ideal-gas formulation to compute pressure fields and heat transfer rates for real-gas, hypersonic flowfields has been shown to be useful for preliminary design purposes. The effective-γ procedure requires only 5% of the CPU time needed for a full thermochemical nonequilibrium solution making this procedure ideal for design studies of this nature.

Acknowledgments

Support for Susan Tokarcik and Ethiraj Venkatapathy was provided by NASA Grant NCC2-420. Support for the SAGE grid adaptation program was provided by Carol Davies of Sterling Software.

References

[1]Wang, J. A., and Shih, K. C., "Numerical Studies on Inflatable Ballute as an Aerodynamic Decelerator for a Solid Rocket Motor Hypersonic Re-Entry," AIAA Paper 91-0841, April 1991.

[2]Anon., "Aero-Assist Flight Experiment System Requirement Document," NASA Marshall Space Flight Center, MSFC-RQMT-1439-B, Huntsville, AL, June 1990.

[3]Nerem, R. M., "Pressure and Heat Transfer on High-Speed Aerodynamic Decelerators of the Ballute Type," *Proceedings of the AIAA Aerodynamic Decelerator Systems Conference,* Houston, TX, Sept. 1966, pp. 135–143.

[4]Alexander, W., "Summary of the Development Status of Attached Inflatable Decelerators," AIAA Paper 68-929, Sept. 1968.

[5]Alexander, W., "A Discussion of Governing Decelerator Performance and Design Parameters in the Supersonic Flight Regime," AIAA Paper 68-938, Sept. 1968.

[6]Bohon, H., and Miserentino, R., "Attached Inflatable Decelerator Performance Evaluation and Mission-Application Study," AIAA Paper 70-1163, Sept. 1970.

[7]Aebischer, A., and Suters, E., Jr., "Development Status of Ballute System For Stabilization and Retardation of Aircraft Stores," AIAA Paper 70-1200, Sept. 1970.

[8]Blanco, T., Berman, H., and Steck, H., "Recovery of High Performance Re-Entry Vehicles," *Proceedings of the AIAA Aerodynamic Decelerator Systems Conference,* Houston, TX, Sept. 1966, pp. 73–77.

[9]Ryan, J., "Aerodynamic Deceleration from as High as Mach 4.0 for the ALARR Project," *Proceedings of the AIAA Aerodynamic Decelerator Systems Conference,* Houston, TX, Sept. 1966, pp. 172–180.

[10]Minerva, P., and Turner, R., "Recovery System Requirements for High Performance Re-Entry Vehicle," *Proceedings of the AIAA Aerodynamic Decelerator Systems Conference,* Houston, TX, Sept. 1966, pp. 188–195.

[11]Wyborny, W., and Kabelitz, H., "Comparison of Hypersonic Aerodynamic Deceleration Systems Based on Gun Tunnel Investigations," AIAA Paper 70-1174, Sept. 1970.

[12]Sims, L., and Bursey, C., Jr., "Comparative Performances of Two Hypersonic Deceleration Devices," AIAA Paper 70-1207, Sept. 1970.

[13]Davies, C., and Venkatapathy, E., "A Simplified Self-Adaptive Grid Method, SAGE," NASA TM-102198, Oct. 1989.

[14]Palmer, G., "The Development of an Explicit Thermo-Chemical Nonequilibrium Algorithm and Its Application to Compute Three Dimensional AFE Flowfields," AIAA Paper 89-1701, June 1989.

[15]Park, C., "Assessment of Two Temperature Kinetic Model for Ionizing Air," AIAA Paper 87-1574, July 1987.

[16]Yates, L. A., and Venkatapathy, E., "Trim Angle Measurements in Free-Flight Facilities," AIAA Paper 91-1632, June 1991.

[17]Candler, G., "The Computation of Weakly Ionized Hypersonic Flows in Thermo-Chemical Nonequilibrium," Ph.D. Dissertation, Dept. of Aeronautics and Astronautics, Stanford Univ., Stanford, CA, June 1988.

[18]Delery, J., and Coet, M. C., "Experiments on Shock-Wave/Boundary-Layer Interactions Produced by Two-Dimensional Ramps and Three-Dimensional Obstacles," Workshop on Hypersonic Flows for Re-Entry Problems, Antibes, France, Jan. 1990.

[19]Marvin, J. G., and Deiwert, G. S., "Convective Heat Transfer in Planetary Gases," NASA TR R-244, July 1965.

[20]Tokarcik, S. A., Venkatapathy, E., Candler G., and Palmer, G., "Computational Flow Predictions for Hypersonic Drag Devices," AIAA Paper 91-3303, Sept. 1991.

Michael E. Tauber
Associate Editor